

# Metal Halide Thermoelectrics: Prediction of High-Performance $\text{CsCu}_2\text{I}_3$

Jong Woong Park<sup>1D</sup>,<sup>1</sup> Young-Kwang Jung<sup>1D</sup>,<sup>2,\*</sup> and Aron Walsh<sup>1D</sup>,<sup>3,4,†</sup>

<sup>1</sup>Department of Materials Science and Engineering, Yonsei University, Seoul 03722, South Korea

<sup>2</sup>Department of Chemical Engineering and Biotechnology, University of Cambridge, Cambridge CB3 0AS, United Kingdom

<sup>3</sup>Department of Materials, Imperial College London, Exhibition Road, London SW7 2AZ, United Kingdom

<sup>4</sup>Department of Physics, Ewha Womans University, Seoul 03760, South Korea

(Received 5 May 2023; revised 8 August 2023; accepted 24 August 2023; published 6 October 2023)

Thermoelectric devices can directly convert waste heat into electricity, which makes them an important clean energy technology. The underlying materials performance can be evaluated by the dimensionless figure of merit  $ZT$ . Metal halides are attractive candidates due to their chemical flexibility and ease of processing; however, the maximum  $ZT$  realized ( $ZT = 0.15$ ) falls far below the level needed for commercialization ( $ZT > 1$ ). Using a first-principles procedure, we assess the thermoelectric potential of copper halide  $\text{CsCu}_2\text{I}_3$ , which features one-dimensional Cu-I connectivity. The  $n$ -type crystal is predicted to exhibit a maximum  $ZT$  of 2.2 at 600 K along the  $b$  axis. The strong phonon anharmonicity of this system is shown by locally stable noncentrosymmetric  $Amm2$  structures that are averaged to form the observed centrosymmetric  $Cmcm$  space group. Our work provides insights into the structure-property relations in metal halide thermoelectrics and suggests a path forward to engineer higher-performance heat-to-electricity conversion.

DOI: 10.1103/PRXEnergy.2.043004

## I. INTRODUCTION

Thermoelectric materials—which enable the direct conversion of waste heat to electricity—have received great attention as one of the most promising renewable energy technologies [1]. The performance of thermoelectric materials is evaluated by the dimensionless figure of merit,  $ZT$ :

$$ZT = \frac{S^2 \sigma T}{\kappa_{\text{elec}} + \kappa_{\text{latt}}}. \quad (1)$$

Here  $S$  is the Seebeck coefficient,  $\sigma$  is the electrical conductivity,  $T$  is the temperature,  $\kappa_{\text{elec}}$  is the electronic thermal conductivity, and  $\kappa_{\text{latt}}$  is the lattice thermal conductivity [the power factor (PF) is defined as  $S^2 \sigma$ ]. Because of the recent progress in calculation methods for electron (hole) and phonon transport in solid crystals, computational studies have sought to discover novel compounds that possess a high  $ZT$  [2–5]. Although the trade-off effect

between the parameters that control  $ZT$  makes the optimization challenging, search for an intrinsically low  $\kappa_{\text{latt}}$  material is still crucial to maximize performance [6]. In other words, high thermoelectric performance requires the phonons to be disrupted like in a glass but the electrons to have a high mobility like in crystalline semiconductors (i.e., phonon-glass electron crystal) [7].

### A. Metal halide thermoelectrics

Metal halides have been studied for their uses in various applications, including solar cells [8,9], light-emitting diodes [10,11], and memristors [12,13]. These materials are also known to have an intrinsically “ultralow”  $\kappa_{\text{latt}}$  ( $< 1 \text{ W/m K}$ ) [14–16], and several reports have started to suggest their potential for thermoelectric applications (Table I).

However, the highest maximum  $ZT$  of 0.15 achieved for halide perovskite  $\text{CsSnI}_3$  [18] is far from competing with top thermoelectric materials such as SnSe whose maximum  $ZT$  is  $> 2.6$  [29]. In addition, studies were mainly conducted on conventional halide perovskites, while emerging low-dimensional metal halides have yet to be explored. Recently, we reported a high thermoelectric potential in metal halide  $\text{Cs}_3\text{Cu}_2\text{I}_5$  for the first time where asymmetric heat and charge transport in the material enables a high maximum  $ZT$  of 2.6 at 600 K [28].

\*yj359@cam.ac.uk

†a.walsh@imperial.ac.uk

Published by the American Physical Society under the terms of the Creative Commons Attribution 4.0 International license. Further distribution of this work must maintain attribution to the author(s) and the published article's title, journal citation, and DOI.

TABLE I. Representative works on metal halide studies for thermoelectric devices with their  $\kappa_{\text{latt}}$  and  $ZT$  values. The mentioned values are for room temperature unless indicated otherwise. NW, Nanowire.

	Compound	$\kappa_{\text{latt}}$ (W/m K)	$ZT$	$\kappa$ measurement	Ref.
Conventional perovskites	$\text{CsSnI}_3$	0.38	0.11 (320 K)	NW thermometry	[15]
	$\text{CsSnI}_3$	0.28	0.08 (323 K)	3- $\omega$ method	[17]
	$\text{CsSnI}_3$	0.60	0.15 (550 K)	Laser flash method	[18]
	$\text{CsSnI}_3 + \text{SnCl}_2$ 1%	0.38	0.14 (345 K)	3- $\omega$ method	[19]
	$\text{CsSnI}_3 + \text{PbI}_2$ 0.5%		0.14 (523 K)	Laser flash method	[20]
	$\text{CsSn}_{0.8}\text{Ge}_{0.2}\text{I}_3$		0.12 (473 K)	Laser flash method	[21]
	$\text{CsSnBr}_3$	0.64		Laser flash method	[18]
	$\text{CsPbI}_3$	0.45		NW thermometry	[15]
	$\text{CsPbBr}_3$	0.42		NW thermometry	[15]
	$\text{CsPbBr}_3$	0.44 (tot.)		3- $\omega$ method	[22]
Low-dimensional metal halides	$\text{CsPbBr}_3$	0.46 (tot.)		FDTR	[23]
	$\text{CsPbCl}_3$	0.49 (tot.)		3- $\omega$ method	[24]
	$\text{Cs}_2\text{SnI}_6$	0.29		Laser flash method	[25]
	$\text{Cs}_2\text{SnI}_2\text{Cl}_2$	0.60 (300 K)		Laser flash method	[26]
	$\text{CsPb}_2\text{Br}_5$	0.32 (tot.)		3- $\omega$ method	[22]
	$\text{Cs}_2\text{PbI}_2\text{Cl}_2$	0.45 (300 K)		Laser flash method	[26]
	$\text{Cs}_2\text{PbI}_2\text{Cl}_2$	0.37 (295 K)		Laser flash method	[27]
$\text{Cs}_4\text{PbCl}_6$	$\text{Cs}_4\text{PbCl}_6$	0.30 (tot.)		3- $\omega$ method	[24]
	$\text{Cs}_3\text{Cu}_2\text{I}_5$	0.02	2.6 (600 K)	Phono3py (theory)	[28]
	$\text{CsCu}_2\text{I}_3$	0.05 (300 K)	0.4 (300 K)	Phono3py (theory)	This study
		0.02 (600 K, <i>b</i> axis)	2.2 (600 K, <i>b</i> axis)		

In this article, we present  $\text{CsCu}_2\text{I}_3$  as a candidate for thermoelectric applications on the basis of first-principles predictions.  $\text{CsCu}_2\text{I}_3$  is one of the copper-based low-dimensional halide compounds where one-dimensional (1D)  $[\text{Cu}_2\text{I}_3]^-$  anionic chains are separated by  $\text{Cs}^+$  cations. By performing lattice dynamics simulations, we found that heat transport in the material is highly anisotropic where  $\kappa_{\text{latt}}$  in the *a*-*b* plane (perpendicular to the chains) is about 2 times lower than that along the *c* axis (chain direction). We also confirmed that the experimentally reported *Cmcm* structure of the material is not dynamically stable but an average of *Amm2* structures during our phonon analysis. Interestingly, electron transport in the material shows an opposite anisotropy compared to the phonon transport; electron mobility in the *a*-*b* plane is 1.5 times higher than that along the *c* axis. Because of this unique anisotropy of heat and electron transport in a single material, we predict that  $\text{CsCu}_2\text{I}_3$  in the *Amm2* structure reaches a  $ZT$  of 2.2 at 600 K along the *b* axis, having potential as a next-generation thermoelectric material.

## II. RESULTS AND DISCUSSION

### A. First-principles thermoelectrics workflow

The workflow to predict  $ZT$  from first principles is shown in Fig. 1. In principle, this only requires prior knowledge of a crystal structure and all other properties can be directly calculated in turn. As the first step, the crystal structure of a compound of interest should be optimized to a local minimum in the potential energy surface. If

the compound shows imaginary phonon modes, additional crystal structure optimization and/or anharmonic corrections should be applied to obtain a dynamically stable structure, so that reliable thermal properties can be calculated [30]. With the dynamically stable crystal structure, bulk properties can be assessed. Results from steps 2–4 are given as inputs for calculating carrier lifetimes and transport properties— $S$ ,  $\sigma$ , and  $\kappa_{\text{elec}}$  (step 5), while lattice thermal conductivity  $\kappa_{\text{latt}}$  is obtained from anharmonic phonon calculations (steps 6 and 7). Finally, thermoelectric properties such as  $ZT$  and thermodynamic efficiency ( $\eta$ ) are predicted by combining the outputs from steps 5 and 7. Computational details are provided in Sec. IV.

### B. Structural analysis

$\text{CsCu}_2\text{I}_3$  has been reported in a *Cmcm* space group [31,32], where 1D  $[\text{Cu}_2\text{I}_3]^-$  anionic chains are separated by  $\text{Cs}^+$  cations, as shown in Fig. 2. When the experimentally known structure was adopted and optimized, we found that imaginary phonon modes are persistent across the first Brillouin zone [see Fig. 3(a)], which confirms dynamic structural instability of the *Cmcm* structure. (This will be further discussed in Sec. II C.) To obtain a dynamically stable crystal structure, we deformed the *Cmcm* structure along the eigenvector of its imaginary  $\Gamma$  phonon mode, which results in a structural transition to a new lower-symmetry *Amm2* phase. The structural transition from *Cmcm* to *Amm2* occurs with atomic positions shifted along the directions indicated by the arrows in Figs. 2(a)

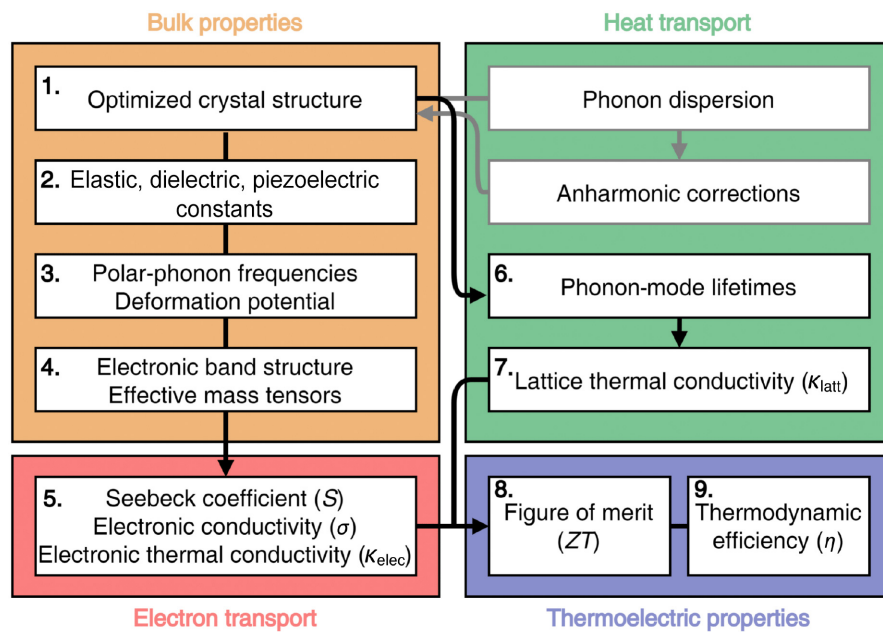


FIG. 1. Diagram for first-principles thermoelectrics assessment workflow (total nine steps). Steps that are optional or only required in certain cases are shown with gray boxes and arrows.

and 2(c). Cs and I atoms move within the  $b$  axis and  $a$ - $b$  plane, respectively, while Cu atoms move along the  $c$  axis. The Cu—I—Cu bond angle for *Cmcm* is alternately  $71.54^\circ$  and  $71.16^\circ$ , while polyhedra distortion in *Amm2* results in bond angles of  $61.39^\circ$  and  $81.42^\circ$ , as shown in Figs. 2(e) and 2(f). In *Cmcm*, the Cu—I bond lengths in the  $[\text{CuI}_4]^{3-}$  tetrahedron are of a similar value (2.62 and 2.61 Å, two each), as opposed to the bonds in *Amm2* all having a different value (2.66, 2.65, 2.58, and 2.61 Å). Thus, while the crystal system is maintained as orthorhombic, the crystal symmetry is lowered from centrosymmetric *Cmcm* to noncentrosymmetric *Amm2*. Comparison of the calculated lattice parameters of *Cmcm* and *Amm2*, as well as the experimental values from X-ray diffraction measurements

are provided in Table II. The structural transition results in  $a_0$  decreasing by 0.30%, while  $b_0$  increases by 0.84%, with both changes due to the movements of Cs and I atoms. In contrast,  $c_0$  is equivalent in both structures, as the shift in Cu atoms evens out macroscopically. *Amm2* has an expanded volume of 0.70% compared to *Cmcm*. The elastic and dielectric tensors calculated from *Cmcm* and *Amm2* phases are provided in the Supplemental Material [34].

### C. Dynamic structural instability

The phonon dispersions of *Cmcm* and *Amm2* are illustrated together with the atom-projected phonon density of states (PDOS) in Fig. 3(a) and 3(b), respectively. While

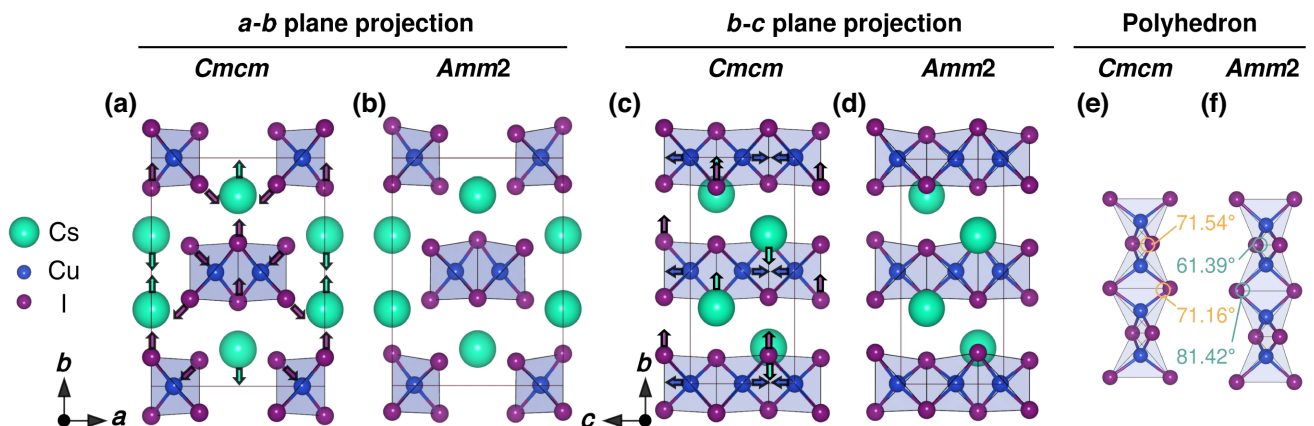


FIG. 2. Projected crystal structure of  $\text{CsCu}_2\text{I}_3$  (a) *Cmcm* and (b) *Amm2* through the  $a$ - $b$  plane, and to the  $b$ - $c$  plane of (c) *Cmcm* and (d) *Amm2*. Arrows indicate the directions that atoms move when the *Cmcm*-to-*Amm2* transition occurs. The maximum atomic displacement during the transition is from the Cu atoms (0.22 Å). Polyhedron analysis of (e) *Cmcm* and (f) *Amm2*. Cu—I—Cu bond angles of each structure are indicated.

TABLE II. Calculated lattice parameters ( $a_0$ ,  $b_0$ ,  $c_0$ ) and volume ( $V_0$ ) of the conventional orthorhombic unit cell for both polymorphs of  $\text{CsCu}_2\text{I}_3$ , and the experimental values from X-ray diffraction measurements.

	$a_0$ (Å)	$b_0$ (Å)	$c_0$ (Å)	$V_0$ (Å $^3$ )
<i>Cmcm</i>	10.06	13.08	6.10	802.3
<i>Amm2</i>	10.03	13.19	6.10	807.9
Expt. [33]	10.55	13.17	6.10	847.4

the Materials Project [35] repository, as well as computational [36] and experimental [33] reports, indicate  $\text{CsCu}_2\text{I}_3$  as a *Cmcm* structure, dynamic structural instability of *Cmcm* is evident by the numerous imaginary modes shown in Fig. 3(a). The eigenvector components for the imaginary mode at the  $\Gamma$  point of *Cmcm* are shown by arrows in Figs. 2(a) and 2(c). Using ModeMap [37], the corresponding energy as a function of the distortion amplitude along the eigenvectors illustrated in Figs. 2(a) and 2(c) is shown in Fig. 4. A characteristic double-well potential-energy curve is shown. The saddle point corresponds to the *Cmcm* structure, while the two wells indicate the lower symmetry *Amm2* structure as a local minimum. Thus, the energy-lowering distortion causes a structural transition to a ground-state polymorph, *Amm2*, with an energy 2.84 meV/atom lower than *Cmcm*. As shown in Fig. 3(b), the absence of imaginary phonon modes indicates the dynamic stability of *Amm2*. However, as the depth of the potential energy well is relatively shallow, the well would be easily filled at room temperature ( $k_B T \sim 25.7$  meV), and at this state a mixture of *Amm2* and *Cmcm* structures would exist. Hence, we propose that the previously reported centrosymmetric *Cmcm* structure is a macroscopic average over locally noncentrosymmetric *Amm2* structures. This

phenomenon is similar to the case of SnSe, where the superposition of the locally ordered structure (*Pnma*) leads to the average structure (*Cmcm*) [38]. The simulated XRD patterns of the *Cmcm* and *Amm2* structures are displayed in Fig. S1 within the Supplemental Material [34]. As anticipated, additional peaks corresponding to the *Amm2* structure are observed. However, the intensity ratio of these peaks to the main ones is significantly low. This makes it difficult to distinguish them, particularly given the typical signal-to-noise ratio associated with standard XRD techniques. In addition, in the *Amm2* structure, a lack of inversion symmetry causes a spontaneous electric polarization. As shown in Figs. 2(a) and 2(c), polarization mainly occurs within the  $a$ - $b$  plane by the shift of Cs and I atoms, while minute polarization along the  $c$  axis corresponds to the movement of Cu atoms. The corresponding piezoelectric tensor of the *Amm2* structure is provided in Table S1 within the Supplemental Material [34].

#### D. Ultralow lattice thermal conductivity

Figure 5 shows the  $\kappa_{\text{latt}}$  of *Amm2*  $\text{CsCu}_2\text{I}_3$ , as a function of temperature along different crystallographic directions. Because  $\text{CsCu}_2\text{I}_3$  is experimentally reported to have a melting point at about 644 K [33,39], the temperature range for calculating  $\kappa_{\text{latt}}$  as well as transport and thermoelectric properties discussed later is set up to 600 K. *Amm2* shows an unexpectedly low  $\kappa_{\text{latt}}$  (i.e., ultralow  $\kappa_{\text{latt}}$ ) of a value under 0.1 W/m K for all directions even at 300 K; 0.05, 0.03, and 0.08 W/m K for the  $a$ ,  $b$ , and  $c$  axes, respectively. The isotropically averaged  $\kappa_{\text{latt}}$  ( $\kappa_{\text{avg}}$ ) at 300 K is 0.05 W/m K, which is lower than one of the top thermoelectric materials, SnSe (0.2 W/m K at 300 K [40]). The value is slightly higher compared to  $\text{Cs}_3\text{Cu}_2\text{I}_5$  ( $\kappa_{\text{avg}} =$

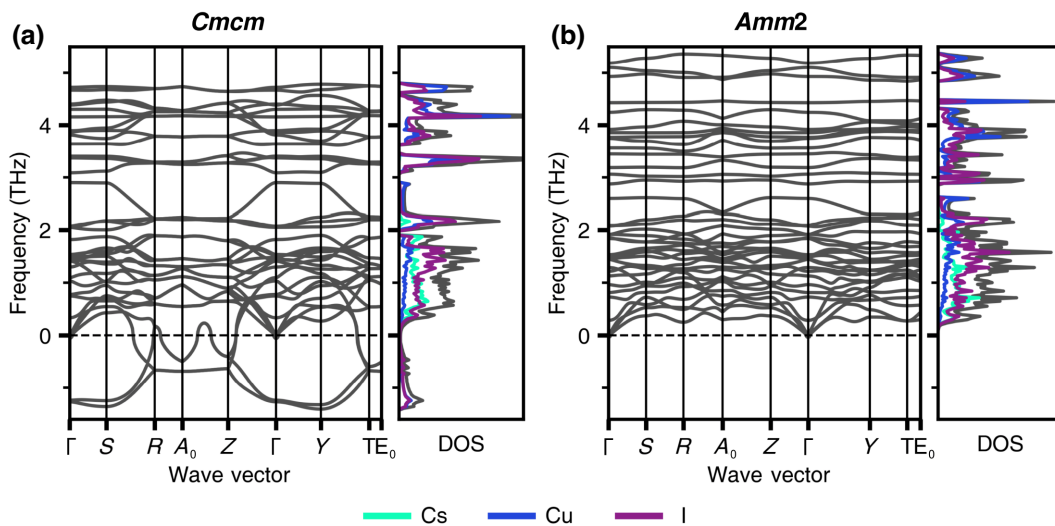


FIG. 3. Phonon dispersions of  $\text{CsCu}_2\text{I}_3$  in (a) *Cmcm* and (b) *Amm2* structures. The atom-projected phonon density of states is plotted to the right of the phonon dispersion.

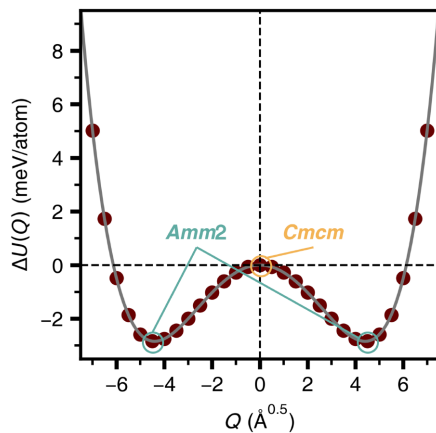


FIG. 4. Potential energy surface along the eigenvector components [arrows in Figs. 2(a) and 2(c)] for the imaginary mode at the  $\Gamma$  point of the phonon band structure of *Cmcm*  $\text{CsCu}_2\text{I}_3$ . Filled circles represent calculated data points, and the solid line is a fit to a polynomial function.

0.02 W/m K at room temperature [28]), which was calculated at a similar level of theory. At 600 K, the  $\kappa_{\text{latt}}$  values are 0.02 W/m K along the *a* and *b* axes, and 0.04 W/m K along the *c* axis ( $\kappa_{\text{avg}}$  being 0.03 W/m K). The anisotropy of  $\text{CsCu}_2\text{I}_3$ , having a higher  $\kappa_{\text{latt}}$  along the *c* axis, can be ascribed to a weaker chemical bonding towards the *c* axis of the unit cell [41]. It is worth noting that the *c* axis is parallel to the  $[\text{Cu}_2\text{I}_3]^-$  chains.

Acoustic phonon modes and low-frequency optic modes act as the primary heat carriers in crystals, mainly contributing to  $\kappa_{\text{latt}}$ . As shown in Fig. 3(b), the low-lying optic modes of *Amm2* are relatively flat, which leads to low group velocities ( $v_\lambda$ ), one of the reasons for its ultralow  $\kappa_{\text{latt}}$ . In addition, the high density of the low-lying optic modes produces a large number of scattering channels at this frequency range, causing short phonon lifetimes ( $\tau_\lambda$ ).

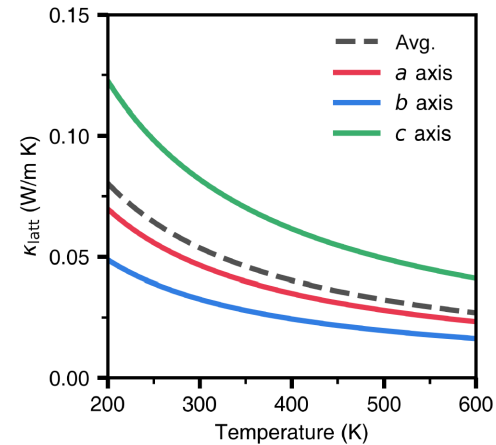


FIG. 5. Lattice thermal conductivity ( $\kappa_{\text{latt}}$ ) of the  $\text{CsCu}_2\text{I}_3$ , *Amm2* structure, as a function of temperature along different crystallographic axes. “Avg.” refers to the isotropically averaged  $\kappa_{\text{latt}}$  ( $\kappa_{\text{avg}}$ ) along the three (*a*, *b*, and *c*) axes.

Figure S2 within the Supplemental Material [34] shows avoided crossings of the acoustic and low-frequency optic modes along the  $\Gamma$ –Y direction. Avoided crossing is a characteristic feature shown when a “rattler” is present in the material [42]. PDOS shown in Fig. 3(b) indicates that lower-frequency phonon modes mostly comprise motions of Cs atoms. Thus, we can infer that Cs atoms behave as the rattler, rattling within the space between  $[\text{Cu}_2\text{I}_3]^-$  chains. Figure S3 within the Supplemental Material [34] shows the Cs–I bonds (total ten), and the broad range of bond lengths from 3.81 to 4.21 Å contributes to the anharmonicity of  $\text{CsCu}_2\text{I}_3$ . This is similar to the origin of anharmonicity of SnSe [43]. We note that fluctuations between *Cmcm* and *Amm2* could also contribute to the scattering of the heat transport, but such higher-order anharmonicity is not considered here.

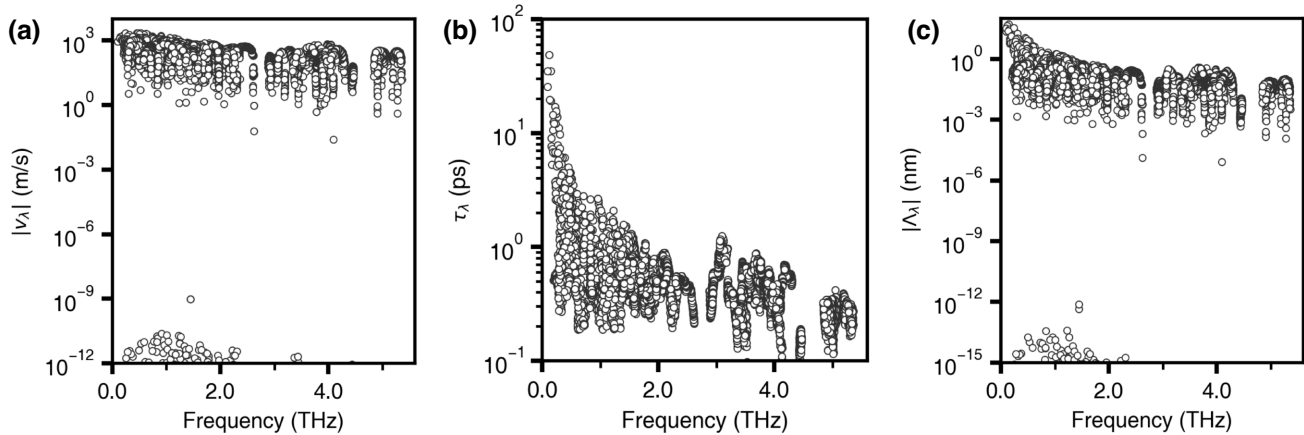


FIG. 6. Modal properties of the lattice thermal conductivity ( $\kappa_{\text{latt}}$ ) of the  $\text{CsCu}_2\text{I}_3$  *Amm2* structure at 300 K: (a) group velocity norms ( $v_\lambda$ ), (b) lifetimes ( $\tau_\lambda$ ), and (c) mean free paths ( $\Lambda_\lambda = v_\lambda \times \tau_\lambda$ ).

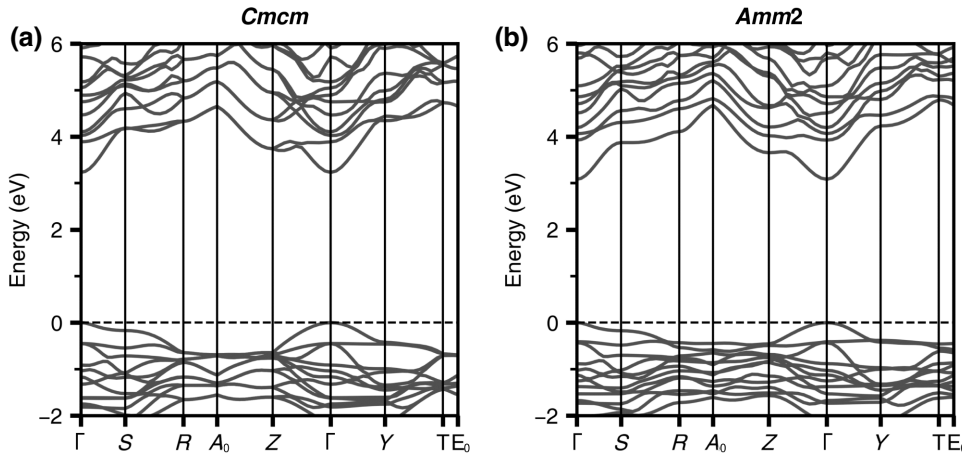


FIG. 7. Electronic band structures of (a) *Cmcm* and (b) *Amm2*  $\text{CsCu}_2\text{I}_3$ , (a) *Cmcm* and (b) *Amm2* structure (the valence band maximum is set to 0 eV).

To further understand the origins of the ultralow  $\kappa_{\text{latt}}$  of  $\text{CsCu}_2\text{I}_3$ , we analyzed the modal contributions to the net transport (Fig. 6). The net transport  $\kappa_{\text{latt}}$  is a sum of the individual phonon modes ( $\lambda$ ):

$$\kappa_{\text{latt}} = \frac{1}{NV_0} \sum_{\lambda} \kappa_{\lambda} = \frac{1}{NV_0} \sum_{\lambda} C_{\lambda} v_{\lambda} \otimes v_{\lambda} \tau_{\lambda}. \quad (2)$$

Here  $N$  is the number of unit cells in the crystal (equivalent to the number of wave vectors included in the Brillouin zone summation),  $V_0$  is the volume of the crystallographic unit cell, and  $C_{\lambda}$  is the modal heat capacity. The frequency spectra of  $v_{\lambda}$ ,  $\tau_{\lambda}$ , and the phonon mean free path ( $\Lambda_{\lambda} = v_{\lambda} \times \tau_{\lambda}$ ) at 300 K are shown in Figs. 6(a)–6(c), respectively [44]. In the entire frequency range, the majority of  $v_{\lambda}$  falls within the range 1– $10^3$  m/s, and the fastest modes are seen in the 0–0.2-THz frequency range. The fastest modes correspond to the acoustic phonon bands that are relatively dispersive compared to the optic modes. The overall spectra are comparable to  $(\text{CH}_3\text{NH}_3)\text{PbI}_3$  (MAPbI<sub>3</sub>) [45], a 3D perovskite reported to have an ultralow  $\kappa_{\text{latt}}$  of 0.05 W/m K at 300 K, while the fastest modes have a lower  $v_{\lambda}$  in  $\text{CsCu}_2\text{I}_3$ . In addition, a number of modes have a very low  $v_{\lambda}$ , from  $10^{-12}$  to  $10^{-10}$  m/s, unseen in the  $v_{\lambda}$  spectra of MAPbI<sub>3</sub> [45] and  $\text{Cs}_3\text{Cu}_2\text{I}_5$  [28]. These modes correspond to the low-lying optic modes in the 0.2–2.4-THz frequency range that are relatively flat. The low  $v_{\lambda}$  is attributed to the heavy elements that constitute  $\text{CsCu}_2\text{I}_3$ .

Lifetimes  $\tau_{\lambda}$  mostly fall within the range  $10^{-1}$ – $10^1$  ps, while a number of phonon modes within the 0–0.2-THz frequency range (acoustic phonon modes) have a  $\tau_{\lambda}$  longer than 10 ps. The overall spectra is similar to MAPbI<sub>3</sub> [45] and  $\text{Cs}_3\text{Cu}_2\text{I}_5$  [28], while the longest  $\tau_{\lambda}$  of  $\text{CsCu}_2\text{I}_3$  are longer compared to  $\text{Cs}_3\text{Cu}_2\text{I}_5$  (longest being 11 ps). The combination of a low  $v_{\lambda}$  and  $\tau_{\lambda}$  leads to the majority of the modes having  $\Lambda_{\lambda}$  shorter than  $10^0$  nm, which is why  $\text{CsCu}_2\text{I}_3$  shows an ultralow  $\kappa_{\text{latt}}$ . The low-frequency modes

(acoustic and low-lying optic modes) have a relatively faster  $v_{\lambda}$  and longer  $\tau_{\lambda}$ , resulting in a longer  $\Lambda_{\lambda}$  compared to the high-frequency modes. This matches with the fact that acoustic and low-lying optic modes are the primary heat carriers.

### E. Electronic structure and transport properties

The electronic band structures of *Cmcm* and *Amm2* are illustrated in Figs. 7(a) and 7(b), respectively. Both *Cmcm* and *Amm2* phases have a direct band gap ( $E_g$ ) at the  $\Gamma$  point, with  $E_g$  values of 3.23 and 3.08 eV, respectively. The calculated  $E_g$  is similar to the experimental value estimated from the optical absorption spectrum, 3.49 eV [39]. As shown in Fig. S4 within the Supplemental Material [34], upper valence bands are dominated by Cu 3d and I 5p orbitals, while lower conduction bands arise from the

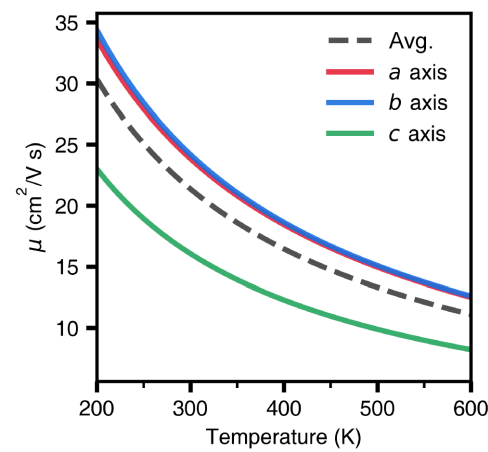


FIG. 8. Mobility ( $\mu$ ) of the  $\text{CsCu}_2\text{I}_3$  *Amm2* structure, as a function of temperature along different crystallographic axes. “Avg.” refers to the isotropically averaged  $\mu$  along the three (*a*, *b*, and *c*) axes (electron concentration of  $6 \times 10^{18} \text{ cm}^{-3}$ ).

hybridization of Cu 4s and I 5p orbitals. For the conduction band minimum, I 5s contributes more compared to I 5p. Calculation of the orbitals that comprise band edges are in good agreement with previous reports [33,39]. The contribution of Cs orbitals on those band edges is negligible, which is the well-known feature of low-dimensional metal halides [46,47]. The corresponding orbitals are also equivalent to the electronic band structure of  $\text{Cs}_3\text{Cu}_2\text{I}_5$  [28]. The upper valence band is relatively flat, having a hole effective mass of  $0.83 m_e$  at the valence band maximum, while the lower conduction band is relatively dispersive with an electron effective mass of  $0.31 m_e$  at the conduction band minimum. The conduction band has multiple valleys ( $\Gamma$  point, Z point, and along the S-R and Y-T directions), and the energy difference between the first and second conduction band edges is 0.57 eV for *Amm2*. The dispersive nature and multiple valleys lead to a high  $\sigma$  and  $S$ , respectively, suggesting the possibility of  $\text{CsCu}_2\text{I}_3$  as a promising *n*-type thermoelectric material.

Figure 8 shows the calculated electron mobility  $\mu$  of *Amm2* as a function of temperature along different crystallographic directions at the optimal electron concentration  $n_e$  ( $6 \times 10^{18} \text{ cm}^{-3}$ ) at which thermoelectric properties are maximized [ $n_e$  will be further discussed in Fig. 10(a) below]. Similar to  $\kappa_{\text{latt}}$ ,  $\mu$  is anisotropic, with  $\mu$  being lower along the  $c$  axis. The isotropically averaged  $\mu$  is  $21.4 \text{ cm}^2/\text{V s}$  at 300 K, which is slightly higher than the  $\mu$  of  $\text{Cs}_3\text{Cu}_2\text{I}_5$  [28] ( $18.2 \text{ cm}^2/\text{V s}$  at room temperature). Figure S5 within the Supplemental Material [34] shows  $\mu$  of *Cmcm* and *Amm2* by the individual scattering mechanisms. Acoustic deformation potential (ADP), ionized impurity (IMP), and polar optical phonon (POP) scattering mechanisms were considered for both structures, and for *Amm2* (noncentrosymmetric), the piezoelectric (PIE) scattering mechanism was considered as well. Here  $\mu$  is limited by POP scattering for both structures, followed by IMP and ADP scattering. POP scattering is dominant in many of the top thermoelectric materials including SnSe

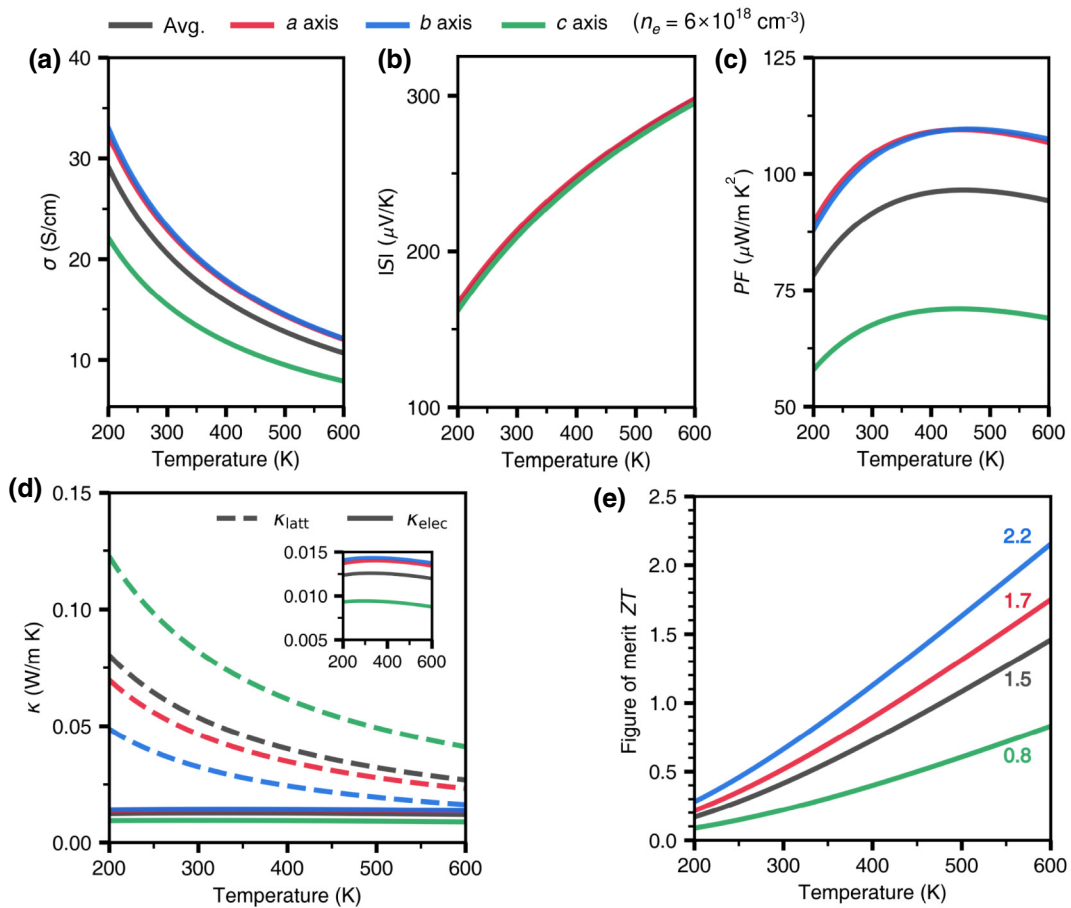


FIG. 9. Transport and thermoelectric properties of the  $\text{CsCu}_2\text{I}_3$  *Amm2* structure, as a function of temperature along different crystallographic axes. (a) Electrical conductivity ( $\sigma$ ); (b) Seebeck coefficient ( $S$ ); (c) power factor ( $\text{PF} = S^2\sigma$ ); (d) electronic ( $\kappa_{\text{elec}}$ , dashed lines) and lattice ( $\kappa_{\text{latt}}$ , solid lines) thermal conductivities (inset shows an enlarged view of  $\kappa_{\text{elec}}$ ); and (e) figure of merit ( $ZT$ ) (electron concentration of  $6 \times 10^{18} \text{ cm}^{-3}$ ).

[48] and  $\text{Cs}_3\text{Cu}_2\text{I}_5$  [28]. In  $\text{Amm}2$ , PIE scattering has the smallest contribution to the total  $\mu$ , as its polarization is minute.

The electronic transport properties— $\sigma$ ,  $S$ , PF, and  $\kappa_{\text{elec}}$ —of  $\text{Amm}2$  as a function of temperature and  $n_e$  are shown in Fig. S6 within the Supplemental Material [34]. Here  $\sigma$  and  $\kappa_{\text{elec}}$  are proportional to  $n_e$ , but have an inverse relationship with temperature. On the other hand,  $|S|$  is disproportionate with  $n_e$ , and increases with temperature. Figure 9 shows  $\sigma$ ,  $S$ , PF, and  $\kappa_{\text{elec}}$  as a function of temperature along different crystallographic directions ( $n_e = 6 \times 10^{18} \text{ cm}^{-3}$ );  $\sigma$ ,  $\kappa_{\text{elec}}$ , and PF are higher along the  $a$  and  $b$  axes, which reflects the anisotropy of  $\mu$ ;  $|S|$  is almost equivalent along all axes. Along the  $b$  axis, PF goes up to  $109.66 \mu\text{W/m K}^2$  at  $470 \text{ K}$ .

## F. Thermoelectric properties

By combining the phonon and electron transport properties using Eq. (1),  $ZT$  for  $\text{CsCu}_2\text{I}_3$  as a function of temperature along different crystallographic axes is predicted [Fig. 9(e)]. Because of the anisotropy of  $\sigma$ ,  $\kappa_{\text{latt}}$ , and  $\kappa_{\text{elec}}$ ,  $ZT$  is also anisotropic, showing a lower value along the  $c$  axis. At  $600 \text{ K}$ , it reaches a value of 2.2 along the  $b$  axis, while the  $a$  and  $c$  axes have a  $ZT$  of 1.7 and 0.8, respectively. Notably, a high  $ZT$  is obtained at a lower temperature compared to the state-of-the-art thermoelectric material,  $n$ -type SnSe, which has a  $ZT$  of 2.0 above  $700 \text{ K}$  [49]. The origin of a high  $ZT$  is a combination of ultralow  $\kappa_{\text{latt}}$  and high PF. Figure 10(a) shows the isotropically averaged  $ZT$  of  $\text{CsCu}_2\text{I}_3$  as a function of temperature and  $n_e$ . The figure of merit  $ZT$  is maximized at  $n_e = 6 \times 10^{18} \text{ cm}^{-3}$ , and the maximum  $ZT$  achievable

at this condition is 1.5 at  $600 \text{ K}$ . As mentioned above, the highest  $ZT$  from a conventional halide perovskite was only 0.15, so this work may derive more attention towards  $\text{CsCu}_2\text{I}_3$  and other low-dimensional metal halides.

The thermodynamic efficiency  $\eta$  of thermoelectric generators can be calculated as

$$\eta = \frac{T_H - T_C}{T_H} \frac{\sqrt{1 + \bar{ZT}} - 1}{\sqrt{1 + \bar{ZT}} + T_C/T_H}, \quad (3)$$

where  $T_H$  and  $T_C$  are the hot side and cold side temperatures of the generator, respectively. The average  $ZT$  ( $\bar{ZT}$ ) is defined as

$$\bar{ZT} = \frac{1}{(T_H - T_C)} \int_{T_C}^{T_H} ZT dT. \quad (4)$$

Using these equations, we plotted  $\eta$  as a function of  $T_H$ , while  $T_C$  is fixed to  $200 \text{ K}$  [Fig. 10(b)]. A maximum  $\eta$  of 13.1% is achieved when the temperature difference is  $400 \text{ K}$  ( $T_H = 400 \text{ K}$ ), and  $\bar{ZT}$  is 0.8.

The main concern when fabricating  $\text{CsCu}_2\text{I}_3$  for thermoelectric applications would be whether the optimal  $n_e$  could be achieved by doping. Currently, doping of low-dimensional metal halides is underexplored, but below we address some of the doping strategies that can be implemented. Similar to the doping approaches of 3D perovskites, doping in low-dimensional metal halides could be achieved by either (1) adding dopant sources to the precursor solution, (2) postsynthesis solution doping or (3) postsynthesis vapor doping [50]. The specific methods could be adding atomic dopants, and molecular dopants

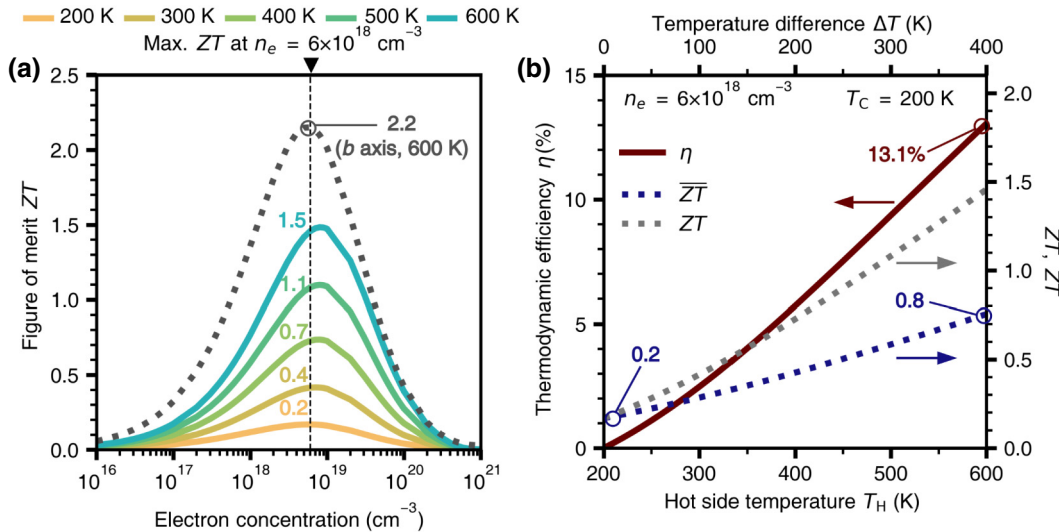


FIG. 10. (a) Calculated figure of merit ( $ZT$ ) as a function of electron concentration and temperature. Isotropically averaged  $ZT$  are given by solid lines, and  $ZT$  along the  $b$  axis (at  $600 \text{ K}$ ) by the gray dotted line. (b) Thermodynamic efficiency ( $\eta$ , red), average  $ZT$  ( $\bar{ZT}$ , blue), and  $ZT$  (gray) as a function of the hot side temperature,  $T_H$ , of the  $\text{CsCu}_2\text{I}_3$   $\text{Amm}2$  structure.

by surface doping. The Cu atoms of  $\text{CsCu}_2\text{I}_3$  mainly contribute to the edge of the band structure [50] (cf. Fig. S4 within the Supplemental Material [34]). Thus, substituting  $\text{Cu}^+$  with +2 charged ions is more likely to produce the necessary states to tune  $n_e$ , compared to the doping of Cs and I.

Another crucial factor when making a thermoelectric module out of a material is the stability of its bulk form. Several experimental studies have synthesized single crystal  $\text{CsCu}_2\text{I}_3$  and verified its air stability, the longest being up to 45 d while maintaining high phase purity and crystalline quality [47,51,52]. Excellent thermal stability up to 614 K without phase change is also verified via differential scanning calorimetry [33]. Therefore, combined with encapsulation technologies to enhance oxygen and moisture resistance, it is expected that stable thermoelectric generators are feasible.

The figure of merit  $ZT$  of  $\text{CsCu}_2\text{I}_3$  is relatively low compared to  $\text{Cs}_3\text{Cu}_2\text{I}_5$ . However, it is reported that  $\text{CsCu}_2\text{I}_3$  is more stable than  $\text{Cs}_3\text{Cu}_2\text{I}_5$  when dopants are added, and the unstable  $\text{Cs}_3\text{Cu}_2\text{I}_5$  decompose and form  $\text{CsCu}_2\text{I}_3$  [53]. Thus, although a higher optimal  $n_e$  is required for  $\text{CsCu}_2\text{I}_3$  ( $6 \times 10^{18} \text{ cm}^{-3}$ , compared to  $4 \times 10^{18} \text{ cm}^{-3}$  for  $\text{Cs}_3\text{Cu}_2\text{I}_5$ ), it may be achieved more easily. In addition, whether this high thermoelectric performance is shown only for  $\text{CsCu}_2\text{I}_3$  and  $\text{Cs}_3\text{Cu}_2\text{I}_5$ , or from low-dimensional metal halides in general, requires further investigation. Through our initial calculations, copper-based metal halides  $\text{K}_2\text{CuX}_3$  and  $\text{CsCu}_2\text{X}_3$  ( $X = \text{Cl}, \text{Br}$ ) are also expected to have a high potential as an  $n$ -type thermoelectric material. Changing the alkali metals or halogens to those in the same group of the periodic table is also worth a try. Thus, investigating  $\text{Cs}_3\text{Cu}_2\text{X}_5$  and  $\text{Rb}_2\text{CuX}_3$  ( $X = \text{Cl}, \text{Br}$ ) as well as  $\text{RbCu}_2\text{Y}_3$  ( $Y = \text{Br}, \text{I}$ ) could be possible.

### III. CONCLUSIONS

In this paper, we reported a new direction for metal halide thermoelectrics with a predictive study on the structure, properties, and performance of  $\text{CsCu}_2\text{I}_3$ .

The dynamic structural instability of the previously known  $Cmcm$  structure of  $\text{CsCu}_2\text{I}_3$  was investigated. We reported a new, ground-state  $Amm2$  structure of  $\text{CsCu}_2\text{I}_3$  and compared its basic bulk properties with  $Cmcm$ . The ultralow  $\kappa_{\text{latt}}$  of  $Amm2$  and its origins were studied in detail. Additionally, the electronic transport properties as well as  $ZT$  were first reported in this work. We predict that  $\text{CsCu}_2\text{I}_3$  is a new promising  $n$ -type thermoelectric material, and require further investigations in low-dimensional metal halides.

The centrosymmetric  $Cmcm$  structure is a macroscopic average over locally noncentrosymmetric  $Amm2$  structures. The octahedra distortion leads to an energy-lowering structural transition from  $Cmcm$  to  $Amm2$ , the energy being

2.84 meV/atom lower. The lack of inversion symmetry in  $Amm2$  results in a spontaneous lattice polarization mainly within the  $a$ - $b$  plane.

$Amm2$  shows an ultralow  $\kappa_{\text{latt}}$  with  $\kappa_{\text{avg}}$  at 300 K of 0.05 W/m K, with the values being higher along the  $c$  axis (i.e., anisotropic). The low  $v_\lambda$  is due to the low-frequency optic modes being relatively flat. Avoided crossings of the acoustic and low-lying optic modes are shown from the dispersion, which is the cause of short  $\tau_\lambda$ . Cs atoms between the  $[\text{Cu}_2\text{I}_3]^-$  chains behave as rattlers, and the inequivalent Cs—I bond lengths give rise to a strong anharmonicity. The structural transition between  $Cmcm$  and  $Amm2$  could also contribute to the phonon scattering.

The conduction band of  $\text{CsCu}_2\text{I}_3$  is relatively dispersive and has multiple valleys, which is the reason for its high  $\sigma$  and  $S$ , respectively, characteristics of a novel  $n$ -type thermoelectric material. POP is the dominant scattering mechanism for both  $Cmcm$  and  $Amm2$ , and PIE scattering is also considered in  $Amm2$  because of its lack of inversion symmetry. Similar to  $\kappa_{\text{latt}}$ , the electronic properties are also anisotropic (superior along the  $a$  and  $b$  axes).

The predicted  $ZT$  of  $\text{CsCu}_2\text{I}_3$  reaches 2.2 at 600 K along the  $b$  axis ( $n_e = 6 \times 10^{18} \text{ cm}^{-3}$ ), comparable to the  $ZT$  of state-of-the-art thermoelectric materials. The origin of high  $ZT$  is a combination of ultralow  $\kappa_{\text{latt}}$  and high PF. A thermodynamic efficiency  $\eta$  of 13.1% is achievable when  $\text{CsCu}_2\text{I}_3$  is used in a thermoelectric generator ( $T_H = 600 \text{ K}$ ,  $T_C = 200 \text{ K}$ ).

## IV. METHODS

### A. Density functional theory calculations

Calculations of the total energy, electronic band structure, and inputs for the AMSET package such as the dielectric, elastic, and piezoelectric constants were performed using density functional theory (DFT) within periodic boundary conditions through the Vienna *ab initio* simulation package (VASP) [54,55]. The projector-augmented-wave (PAW) [56,57] method was employed to explicitly treat the valence states of Cs, Cu, and I atoms as 9 ( $5s^2 5p^6 6s^1$ ), 17 ( $2p^6 3d^{10} 4s^1$ ), and 7 ( $5s^2 5p^5$ ) electrons, respectively.

For structure optimization, the Perdew-Burke-Ernzerhof exchange-correlation functional revised for solids (PBEsol) [58] was used with a  $6 \times 6 \times 8$   $\Gamma$ -centered  $k$  mesh, a plane-wave kinetic energy cutoff of 700 eV, and the convergence criteria set to  $10^{-8}$  eV and  $10^{-4}$  eV/ $\text{\AA}$  for the total energy and atomic forces, respectively. The elastic and dielectric constant was calculated using the finite-displacement (FD) method and density functional perturbation theory, respectively. The bulk modulus was calculated using the Phonopy [59] code by fitting the energy volume to the third-order Birch-Murnaghan equation of state [60].

Calculations of the electronic band structure and electron transport were done using the hybrid DFT functional

of Heyd, Scuseria, and Ernzerhof (HSE06) [61]. Compared to the structure optimization, a denser  $k$  mesh of  $12 \times 12 \times 16$  was used, while the kinetic energy cutoff was lowered to 400 eV. The hole and electron effective mass,  $m^*$ , was calculated using the sumo [62] code, which uses parabolic fitting by the equation

$$\frac{1}{m^*} = \frac{\partial^2 E(k)}{\partial k^2} \frac{1}{\hbar^2}, \quad (5)$$

where  $E(k)$  is the band energy as a function of the electron wave vector  $k$ , and  $\hbar$  is the reduced Plank constant. The electronic band structure calculated above was used as the input.

## B. Structure distortion

Harmonic-level phonon calculations were performed using the Phonopy [59] code with VASP as the force calculator. The second-order interatomic force constants (IFCs) were computed using the supercell FD approach with a  $3 \times 3 \times 3$   $k$  mesh of step size 0.01 Å. A total of 11 displacements for *Cmcm* and 22 displacements for *Amm2* were calculated. A  $2 \times 2 \times 3$  supercell of the 12-atom unit cell (144 atoms) was employed for both structures. The ModeMap [37] code was used to compute the displacement of the atoms,  $u_{j,l}$  ( $j$ th atom in the  $l$ th unit cell), along an imaginary-mode eigenvector,  $W_{\lambda,j}$  ( $\lambda$  is the phonon mode), at the  $\Gamma$  point:

$$u_{j,l} = \frac{1}{\sqrt{n_a m_j}} \Re \left[ \sum_{\lambda} Q_{\lambda} W_{\lambda,j} e^{-iqr_{j,l}} \right]. \quad (6)$$

Here  $m_j$  is the atomic mass,  $n_a$  is the number of atoms in the supercell used to model the displacement,  $Q_{\lambda}$  is the distortion amplitude,  $q$  is the phonon wave vector, and  $r_{j,l}$  is the atomic position. Postprocessing was also performed using the code to map the energy,  $\Delta U(Q)$ , as a function of  $Q_{\lambda}$  along the given  $W_{\lambda,j}$  (cf. Fig. 4). The ground-state structure, *Amm2*, was then obtained using the structure at the energy minimum.

## C. Phonon and electron transport

The  $\kappa_{\text{latt}}$  calculations were carried out using the Phono3py [63] code, solving the linearized Boltzmann transport equation (BTE) using the single-mode relaxation-time approximation (RTA) [Eq. (2)]. The third-order IFCs were calculated with an FD step size of 0.03 Å, and a total of 5568 displacements were considered in a 48-atom unit cell. A  $q$  mesh of  $12 \times 12 \times 16$  was employed to compute the lattice thermal conductivity. Graphical analysis of the modal properties were performed using the Phonopy-power-tool [44] code. Convergence tests for the lattice thermal conductivity over a  $q$  mesh, and distribution of force norms for the force sets can be found in Fig. S7 within the Supplemental Material [34].

Unlike the BoltzTraP [64] code, the AMSET [65] package uses DFT band structures to solve the BTE without the constant RTA. Comparison between computational and experimental values can be found from several studies, which validate the accuracy of the AMSET package [65,66]. Combined with  $\kappa_{\text{latt}}$ , which was calculated at a similar level of theory to our work, the predicted *ZT* values agree well with experimental measurements [66]. The characteristic scattering rate,  $\tau_e$ , is calculated using Matthiessen's rule:

$$\frac{1}{\tau_e} = \frac{1}{\tau^{\text{ADP}}} + \frac{1}{\tau^{\text{IMP}}} + \frac{1}{\tau^{\text{POP}}} + \frac{1}{\tau^{\text{PIE}}}. \quad (7)$$

The mode-dependent scattering rates, from state  $|n\mathbf{k}\rangle$  to state  $|m\mathbf{k} + \mathbf{q}\rangle$ , are calculated using Fermi's golden rule:

$$\tilde{\tau}_{n\mathbf{k} \rightarrow m\mathbf{k} + \mathbf{q}}^{-1} = \frac{2\pi}{\hbar} |g_{nm}(\mathbf{k}, \mathbf{q})|^2 \delta(\varepsilon_{n\mathbf{k}} - \varepsilon_{m\mathbf{k} + \mathbf{q}}) \quad (8)$$

with  $\varepsilon$  the electron energy,  $\delta$  the Dirac delta function, and  $g$  the coupling matrix element. The electron transport properties were computed by the generalized transport coefficients

$$L_{\alpha\beta}^n = e^2 \int \sum_{\alpha\beta} (\varepsilon)(\varepsilon - \varepsilon_F)^n \left[ -\frac{\partial f^0}{\partial \varepsilon} \right] d\varepsilon, \quad (9)$$

where  $\alpha$  and  $\beta$  denote Cartesian coordinates,  $\Sigma_{\alpha\beta}(\varepsilon)$  is the spectral conductivity,  $\varepsilon_F$  is the Fermi level at a certain doping concentration and temperature, and  $f^0$  is the Fermi-Dirac distribution. The properties are obtained as

$$\sigma_{\alpha\beta} = L_{\alpha\beta}^0, \quad (10)$$

$$S_{\alpha\beta} = \frac{1}{eT} \frac{L_{\alpha\beta}^1}{L_{\alpha\beta}^0}, \quad (11)$$

$$\kappa_{\alpha\beta} = \frac{1}{e^2 T} \left[ \frac{(L_{\alpha\beta}^1)^2}{L_{\alpha\beta}^0} - L_{\alpha\beta}^2 \right]. \quad (12)$$

As mentioned above, the required material parameters such as the dielectric, elastic, and piezoelectric constants, phonon frequencies, and deformation potential were determined by DFT calculations (Table S1 within the Supplemental Material [34]). As the valence bands are relatively flat, calculations were only conducted under *n*-type doping conditions, in the doping range from  $10^{16}$  to  $10^{21}$ , and the temperature range from 200 to 600 K. The interpolation factor was set to 10 for all AMSET calculations. Convergence tests for the electron transport calculations over a  $k$  mesh and the interpolation factor can be found in Fig. S6 within the Supplemental Material [34].

Spin-orbit coupling (SOC) was not included in calculating the electron transport properties since we confirmed

that the effect of SOC on the electronic band structure is small in this Cu-based compound—unlike Sn- or Pb-based metal halides [67,68], even for the noncentrosymmetric *Amm*2 phase. Figure S8 within the Supplemental Material [34] shows changes in the band structure of *Cmcm* and *Amm*2 CsCu<sub>2</sub>I<sub>3</sub> with and without SOC.

An online repository containing the optimized crystal structures, force constant sets, and raw AMSET input-output files is available from Zenodo [69].

## ACKNOWLEDGMENTS

This work was supported by a National Research Foundation of Korea (NRF) grant funded by the Korean government (Grant No. 2018M3D1A1058536). Via membership of the UK's HEC Materials Chemistry Consortium, which is funded by EPSRC (EP/L000202), this work used the ARCHER2 UK National Supercomputing Service [70]. Y.-K.J. acknowledges UKRI funding for Marie Skłodowska-Curie Actions Postdoctoral Fellowships 2021 (EP/X025756/1).

J.W.P. performed the calculations and data analysis and wrote the original draft under the supervision of Y.-K.J. and A.W., while all authors contributed to discussing the results and refining the text.

The authors declare that they have no competing financial interests or personal relationships that could have influenced the work reported in this paper.

- [1] L. E. Bell, Cooling, heating, generating power, and recovering waste heat with thermoelectric systems, *Science* **321**, 5895 (2008).
- [2] A. Jain, Y. Shin, and K. A. Persson, Computational predictions of energy materials using density functional theory, *Nat. Rev. Mater.* **1**, 15004 (2016).
- [3] P. Gorai, V. Stevanović, and E. S. Toberer, Computationally guided discovery of thermoelectric materials, *Nat. Rev. Mater.* **2**, 17053 (2017).
- [4] K. B. Spooner, A. M. Ganose, W. W. Leung, J. Buckeridge, B. A. Williamson, R. G. Palgrave, and D. O. Scanlon, BaBi<sub>2</sub>O<sub>6</sub>: A promising n-type thermoelectric oxide with the PbSb<sub>2</sub>O<sub>6</sub> crystal structure, *Chem. Mater.* **33**, 18 (2021).
- [5] T. Deng, J. Recatala-Gomez, M. Ohnishi, D. M. Repaka, P. Kumar, A. Suwardi, A. Abutaha, I. Nandhakumar, K. Biswas, M. B. Sullivan, and G. Wu, Electronic transport descriptors for the rapid screening of thermoelectric materials, *Mater. Horiz.* **8**, 2463 (2021).
- [6] S. Hao, V. P. Dravid, M. Kanatzidis, and C. Wolverton, Computational strategies for design and discovery of nanostructured thermoelectrics, *npj Comput. Mater.* **5**, 58 (2019).
- [7] R. D. M., *CRC Handbook of Thermoelectrics* (CRC Press, Boca Raton, 2010).
- [8] A. Kojima, K. Teshima, Y. Shirai, and T. Miyasaka, Organometal halide perovskites as visible-light sensitizers for photovoltaic cells, *J. Am. Chem. Soc.* **131**, 17 (2009).
- [9] B. Lee, C. C. Stoumpos, N. Zhou, F. Hao, C. Malliakas, C.-Y. Yeh, T. J. Marks, M. G. Kanatzidis, and R. P. Chang, Air-stable molecular semiconducting iodosalts for solar cell applications: Cs<sub>2</sub>Snl<sub>6</sub> as a hole conductor, *J. Am. Chem. Soc.* **136**, 43 (2014).
- [10] Z.-K. Tan, R. S. Moghaddam, M. L. Lai, P. Docampo, R. Higler, F. Deschler, M. Price, A. Sadhanala, L. M. Pazos, D. Credgington, F. Hanusch, T. Bein, H. J. Snaith, and R. H. Friend, Bright light-emitting diodes based on organometal halide perovskite, *Nat. Nanotechnol.* **9**, 687 (2014).
- [11] T. Jun, K. Sim, S. Iimura, M. Sasase, H. Kamioka, J. Kim, and H. Hosono, Lead-free highly efficient blue-emitting Cs<sub>3</sub>Cu<sub>2</sub>I<sub>5</sub> with 0D electronic structure, *Adv. Mater.* **30**, 1804547 (2018).
- [12] Z. Xiao, Y. Yuan, Y. Shao, Q. Wang, Q. Dong, C. Bi, P. Sharma, A. Gruverman, and J. Huang, Giant switchable photovoltaic effect in organometal trihalide perovskite devices, *Nat. Mater.* **14**, 193 (2015).
- [13] J.-M. Yang, Y. K. Jung, J. H. Lee, Y. C. Kim, S. Y. Kim, S. Seo, D. A. Park, J. H. Kim, S. Y. Jeong, I. T. Han, and J. H. Park, Asymmetric carrier transport in flexible interface-type memristor enables artificial synapses with sub-femtojoule energy consumption, *Nanoscale Horiz.* **6**, 987 (2021).
- [14] A. Pisoni, J. Jaćimović, O. S. Barišić, M. Spina, R. Gaál, L. Forró, and E. Horváth, Ultra-low thermal conductivity in organic-inorganic hybrid perovskite CH<sub>3</sub>NH<sub>3</sub>PbI<sub>3</sub>, *J. Phys. Chem. Lett.* **5**, 14 (2014).
- [15] W. Lee, H. Li, A. B. Wong, D. Zhang, M. Lai, Y. Yu, Q. Kong, E. Lin, J. J. Urban, J. C. Grossman, and P. Yang, Ultralow thermal conductivity in all-inorganic halide perovskites, *Proc. Natl. Acad. Sci. USA* **114**, 33 (2017).
- [16] M. A. Haque, A. N. Gandi, R. Mohanraman, Y. Weng, B. Davaasuren, A. Emwas, C. Combe, D. Baran, A. Rothenberger, U. Schwingenschlögl, H. N. Alshareef, S. Dong, and T. Wu, A 0D lead-free hybrid crystal with ultralow thermal conductivity, *Adv. Funct. Mater.* **29**, 1809166 (2019).
- [17] W. Tang, T. Liu, and O. Fenwick, High thermoelectric performance based on CsSnI<sub>3</sub> thin films with improved stability, *J. Mater. Chem. A* **10**, 7020 (2022).
- [18] H. Xie, S. Hao, J. Bao, T. J. Slade, G. J. Snyder, C. Wolverton, and M. G. Kanatzidis, All-inorganic halide perovskites as potential thermoelectric materials: Dynamic cation off-centering induces ultralow thermal conductivity, *J. Am. Chem. Soc.* **142**, 20 (2020).
- [19] T. Liu, X. Zhao, J. Li, Z. Liu, F. Liscio, S. Milita, B. C. Schroeder, and O. Fenwick, Enhanced control of self-doping in halide perovskites for improved thermoelectric performance, *Nat. Commun.* **10**, 5750 (2019).
- [20] S. Yu, F. Qian, M. Hu, Z. Ge, J. Feng, and X. Chong, Enhanced thermoelectric performance in inorganic CsSnI<sub>3</sub> perovskite by doping with PbI<sub>2</sub>, *Mater. Lett.* **308**, 131127 (2022).
- [21] F. Qian, M. Hu, J. Gong, C. Ge, Y. Zhou, J. Guo, M. Chen, Z. Ge, N. P. Padture, Y. Zhou, and J. Feng, Enhanced thermoelectric performance in lead-free inorganic CsSn<sub>1-x</sub>Ge<sub>x</sub>I<sub>3</sub> perovskite semiconductors, *J. Phys. Chem. C* **124**, 22 (2020).
- [22] T. Haeger, M. Wilmes, R. Heiderhoff, and T. Riedl, Simultaneous mapping of thermal conductivity, thermal diffusivity,

- and volumetric heat capacity of halide perovskite thin films: A novel nanoscopic thermal measurement technique, *J. Phys. Chem. Lett.* **10**, 11 (2019).
- [23] G. A. Elbaz, W. L. Ong, E. A. Doud, P. Kim, D. W. Paley, X. Roy, and J. A. Malen, Phonon speed, not scattering, differentiates thermal transport in lead halide perovskites, *Nano Lett.* **17**, 9 (2017).
- [24] T. Haeger, M. Ketterer, J. Bahr, N. Pourdavoud, M. Runkel, R. Heiderhoff, and T. Riedl, Thermal properties of  $\text{CsPbCl}_3$  thin films across phase transitions, *J. Phys. Mater.* **3**, 024004 (2020).
- [25] A. Bhui, T. Ghosh, K. Pal, K. S. Rana, K. Kundu, A. Soni, and K. Biswas, Intrinsically low thermal conductivity in the *n*-type vacancy-ordered double perovskite  $\text{Cs}_2\text{SnI}_6$ : Octahedral rotation and anharmonic rattling, *Chem. Mater.* **34**, 7 (2022).
- [26] Z. Zeng, C. Chen, C. Zhang, Q. Zhang, and Y. Chen, Critical phonon frequency renormalization and dual phonon coexistence in layered ruddlesden-popper inorganic perovskites, *Phys. Rev. B* **105**, 184303 (2022).
- [27] P. Acharyya, T. Ghosh, K. Pal, K. Kundu, K. S. Rana, J. Pandey, U. V. Soni, A. Waghmare, and K. Biswas, Intrinsically ultralow thermal conductivity in Ruddlesden-Popper 2D perovskite  $\text{Cs}_2\text{PbI}_2\text{Cl}_2$ : Localized anharmonic vibrations and dynamic octahedral distortions, *J. Am. Chem. Soc.* **142**, 36 (2020).
- [28] Y.-K. Jung, I. T. Han, Y. C. Kim, and A. Walsh, Prediction of high thermoelectric performance in the low-dimensional metal halide  $\text{Cs}_3\text{Cu}_2\text{I}_5$ , *npj Comput. Mater.* **7**, 51 (2021).
- [29] L.-D. Zhao, S.-H. Lo, Y. Zhang, H. Sun, G. Tan, C. Uher, C. Wolverton, V. P. Dravid, and M. G. Kanatzidis, Ultralow thermal conductivity and high thermoelectric figure of merit in SnSe crystals, *Nature* **508**, 373 (2014).
- [30] I. Pallikara, P. Kayastha, J. M. Skelton, and L. D. Whalley, The physical significance of imaginary phonon modes in crystals, *Electron. Struct.* **4**, 033002 (2022).
- [31] N. Jouini, L. Guen, and M. Tournoux, Structure cristalline de  $\text{CsCu}_2\text{I}_3$ , *Rev. Chim. Mineral* **17**, 486 (1980).
- [32] T. Jun, T. Handa, K. Sim, S. Iimura, M. Sasase, J. Kim, Y. Kanemitsu, and H. Hosono, One-step solution synthesis of white-light-emitting films via dimensionality control of the Cs – Cu – I system, *APL Mater.* **7**, 111113 (2019).
- [33] R. Rocanova, A. Yangui, G. Seo, T. D. Creason, Y. Wu, D. Y. Kim, M. H. Du, and B. Saparov, Bright luminescence from nontoxic  $\text{CsCu}_2\text{X}_3$  ( $\text{X} = \text{Cl}, \text{Br}, \text{I}$ ), *ACS Mater. Lett.* **1**, 4 (2019).
- [34] See Supplemental Material at <http://link.aps.org/supplemental/10.1103/PRXEnergy.2.043004> for the calculated bulk properties of both structures; simulated XRD patterns; zoomed phonon dispersion and atom-projected density of states; Cs–I interatomic distances in the *Amm2* structure; electronic band structure of the *Amm2* structure by its individual orbital contribution; calculated electron mobility as a function of temperature; convergence test for calculated transport and thermoelectric properties of the *Amm2* structure; convergence test for calculated lattice thermal conductivity of the *Amm2* structure; and comparison of the spin-orbit coupling effect to the electronic band structure.
- [35] A. Jain, S. P. Ong, G. Hautier, W. Chen, W. D. Richards, S. Dacek, S. Cholia, D. Gunter, D. Skinner, G. Ceder, and K. A. Persson, Commentary: The materials project: A materials genome approach to accelerating materials innovation, *APL Mater.* **1**, 011002 (2013).
- [36] J. Sun and C. A. Ullrich, Optical properties of  $\text{CsCu}_2\text{X}_3$  ( $\text{X} = \text{Cl}, \text{Br}$ , and  $\text{I}$ ): A comparative study between hybrid time-dependent density-functional theory and the Bethe-Salpeter equation, *Phys. Rev. Mater.* **4**, 095402 (2020).
- [37] J. M. Skelton, L. A. Burton, S. C. Parker, A. Walsh, C.-E. Kim, A. Soon, J. Buckeridge, A. A. Sokol, C. R. A. Catlow, A. Togo, and I. Tanaka, Anharmonicity in the high-temperature *Cmcm* phase of SnSe: Soft modes and three-phonon interactions, *Phys. Rev. Lett.* **117**, 075502 (2016).
- [38] B. Jiang, J. Neu, D. Olds, S. A. J. Kimber, K. Page, and T. Siegrist, The curious case of the structural phase transition in SnSe insights from neutron total scattering, *Nat. Commun.* **14**, 3211 (2023).
- [39] S. Cheng, A. Bejtlerova, R. Kucerkova, E. Mihokova, M. Nikl, Z. Zhou, G. Ren, and Y. Wu, Non-hygroscopic, self-absorption free, and efficient 1D  $\text{CsCu}_2\text{I}_3$  perovskite single crystal for radiation detection, *ACS Appl. Mater. Interfaces* **13**, 10 (2021).
- [40] F. Serrano-Sánchez, M. Gharsallah, N. M. Nemes, F. J. Mompean, J. L. Martínez, and J. A. Alonso, Record Seebeck coefficient and extremely low thermal conductivity in nanostructured SnSe, *Appl. Phys. Lett.* **106**, 083902 (2015).
- [41] P. Ying, X. Li, Y. Wang, J. Yang, C. Fu, W. Zhang, X. Zhao, and T. Zhu, Hierarchical chemical bonds contributing to the intrinsically low thermal conductivity in  $\alpha$ -MgAgSb thermoelectric materials, *Adv. Funct. Mater.* **27**, 1604145 (2017).
- [42] W. Rahim, J. M. Skelton, and D. O. Scanlon,  $\text{Ca}_4\text{Sb}_2\text{O}$  and  $\text{Ca}_4\text{Bi}_2\text{O}$ : Two promising mixed-anion thermoelectrics, *J. Mater. Chem. A* **9**, 20417 (2021).
- [43] L. D. Zhao, C. Chang, G. Tan, and M. G. Kanatzidis, SnSe: A remarkable new thermoelectric material, *Energy Environ. Sci.* **9**, 3044 (2016).
- [44] J. M. Skelton, Phono3py-power-tools, <https://github.com/skelton-group/Phono3py-Power-Tools> (accessed 20 March 2022).
- [45] L. D. Whalley, J. M. Skelton, J. M. Frost, and A. Walsh, Phonon anharmonicity, lifetimes, and thermal transport in  $(\text{CH}_3\text{NH}_3)\text{PbI}_3$  from many-body perturbation theory, *Phys. Rev. B* **94**, 220301 (2016).
- [46] Y.-K. Jung, J. Calbo, J.-S. Park, L. D. Whalley, S. Kim, and A. Walsh, Intrinsic doping limit and defect-assisted luminescence in  $\text{Cs}_4\text{PbBr}_6$ , *J. Mater. Chem. A* **7**, 20254 (2019).
- [47] R. Lin, Q. Guo, Q. Zhu, Y. Zhu, W. Zheng, and F. Huang, All-inorganic  $\text{CsCu}_2\text{I}_3$  single crystal with high-PLQY ( $\approx 15.7\%$ ) intrinsic white-light emission via strongly localized 1D excitonic recombination, *Adv. Mater.* **31**, 1905079 (2019).
- [48] J. Ma, Y. Chen, and W. Li, Intrinsic phonon-limited charge carrier mobilities in thermoelectric SnSe, *Phys. Rev. B* **97**, 205207 (2018).
- [49] J. Wei, L. Yang, Z. Ma, P. Song, M. Zhang, J. Ma, F. Yang, and X. Wang, Review of current high-ZT thermoelectric materials, *J. Mater. Sci.* **55**, 12642 (2020).
- [50] E. Amerling, H. Lu, B. W. Larson, A. E. Maughan, A. Phillips, E. Lafalce, L. Whittaker-Brooks, J. J. Berry, M. C.

- Beard, Z. V. Vardeny, and B. J. L., A multi-dimensional perspective on electronic doping in metal halide perovskites, *ACS Energy Lett.* **6**, 3 (2021).
- [51] Z. Li, Z. Li, Z. Shi, and X. Fang, Facet-dependent, fast response, and broadband photodetector based on highly stable all-inorganic  $\text{CsCu}_2\text{I}_3$  single crystal with 1D electronic structure, *Adv. Funct. Mater.* **30**, 2002634 (2020).
- [52] R. Li, Q. Zhu, Q. Guo, Y. Zhu, W. Zheng, and F. Huang, Dual self-trapped exciton emission with ultrahigh photoluminescence quantum yield in  $\text{CsCu}_2\text{I}_3$  and  $\text{Cs}_3\text{Cu}_2\text{I}_5$  perovskite single crystals, *J. Phys. Chem. C* **124**, 20469 (2020).
- [53] R. Fan, S. Fang, S. Liang, Z. Liang, and H. Zhong, Controllable one-step doping synthesis for the white-light emission of cesium copper iodide perovskites, *Photonics Res.* **9**, 5 (2021).
- [54] G. Kresse and J. Furthmüller, Efficient iterative schemes for *ab initio* total-energy calculations using a plane-wave basis set, *Phys. Rev. B* **54**, 11169 (1996).
- [55] G. Kresse and J. Furthmüller, Efficiency of *ab-initio* total energy calculations for metals and semiconductors using a plane-wave basis set, *Comput. Mater. Sci.* **6**, 1 (1996).
- [56] G. Kresse and D. Joubert, From ultrasoft pseudopotentials to the projector augmented-wave method, *Phys. Rev. B* **59**, 1758 (1999).
- [57] P. E. Blöchl, Projector augmented-wave method, *Phys. Rev. B* **50**, 17953 (1994).
- [58] J. P. Perdew, A. Ruzsinszky, G. I. Csonka, O. A. Vydrov, G. E. Scuseria, L. A. Constantin, X. Zhou, and K. Burke, Restoring the density-gradient expansion for exchange in solids and surfaces, *Phys. Rev. Lett.* **100**, 136406 (2008).
- [59] A. Togo and I. Tanaka, First principles phonon calculations in materials science, *Scr. Mater.* **108**, 1 (2015).
- [60] F. Birch, Finite elastic strain of cubic crystals, *Phys. Rev.* **71**, 809 (1947).
- [61] J. Heyd, G. E. Scuseria, and M. Ernzerhof, Hybrid functionals based on a screened Coulomb potential, *J. Chem. Phys.* **118**, 8207 (2003).
- [62] A. M. Ganose, A. J. Jackson, and D. O. Scanlon, sumo: Command-line tools for plotting and analysis of periodic *ab initio* calculations, *J. Open Source Softw.* **3**, 717 (2018).
- [63] A. Togo, L. Chaput, and I. Tanaka, Distributions of phonon lifetimes in Brillouin zones, *Phys. Rev. B* **91**, 094306 (2015).
- [64] G. K. Madsen and D. J. Singh, BoltzTraP. A code for calculating band-structure dependent quantities, *Comput. Phys. Commun.* **175**, 67 (2006).
- [65] A. M. Ganose, J. Park, A. Faghaninia, R. Woodsrobinson, K. A. Persson, and A. Jain, Efficient calculation of carrier scattering rates from first principles, *Nat. Commun.* **12**, 2222 (2021).
- [66] Jan-Hendrik Pöhls, S. Chanakian, J. Park, A. M. Ganose, A. Dunn, N. Friesen, A. Bhattacharya, B. Hogan, S. Bux, A. Jain, A. Mar, and A. Zevalkink, Experimental validation of high thermoelectric performance in  $\text{RECuZnP}_2$  predicted by high-throughput DFT calculations, *Mater. Horiz.* **8**, 209 (2021).
- [67] Y.-K. Jung, J.-H. Lee, A. Walsh, and A. Soon, Influence of Rb/Cs cation-exchange on inorganic Sn halide perovskites: from chemical structure to physical properties, *Chem. Mater.* **29**, 7 (2017).
- [68] A. Amat, E. Mosconi, E. Ronca, C. Quarti, P. Umari, M. K. Nazeeruddin, M. Gratzel, and F. De Angelis, Cation-induced band-gap tuning in organohalide perovskites: Interplay of spin-orbit coupling and octahedra tilting, *Nano Lett.* **14**, 6 (2014).
- [69] <https://doi.org/10.5281/zenodo.8307511>.
- [70] <http://www.archer2.ac.uk>.